A head template for computational dose modelling for transcranial focused ultrasound stimulation

Seyedsina Hosseini [a,b], Oula Puonti [b], Bradley Treeby [c], Lars G. Hanson [a,b], Axel Thielscher [a,b,*]

[a] *Department of Health Technology, Technical University of Denmark, Kgs. Lyngby, Denmark*
[b] *Danish Research Centre for Magnetic Resonance, Centre for Functional and Diagnostic Imaging and Research, Copenhagen University Hospital Amager and Hvidovre, Denmark*
[c] *Department of Medical Physics and Biomedical Engineering, University College London, GowerStreet, London, WC1E 6BT, United Kingdom*

ARTICLE INFO

ABSTRACT

Transcranial focused Ultrasound Stimulation (TUS) at low intensities is emerging as a novel non-invasive brain stimulation method with higher spatial resolution than established transcranial stimulation methods and the ability to selectively stimulate also deep brain areas. Accurate control of the focus position and strength of the TUS acoustic waves is important to enable a beneficial use of the high spatial resolution and to ensure safety. As the human skull causes strong attenuation and distortion of the waves, simulations of the transmitted waves are needed to accurately determine the TUS dose distribution inside the cranial cavity. The simulations require information of the skull morphology and its acoustic properties. Ideally, they are informed by computed tomography (CT) images of the individual head. However, suited individual imaging data is often not readily available. For this reason, we here introduce and validate a head template that can be used to estimate the average effects of the skull on the TUS acoustic wave in the population.

The template was created from CT images of the heads of 29 individuals of different ages (between 20–50 years), gender and ethnicity using an iterative non-linear co-registration procedure. For validation, we compared acoustic and thermal simulations based on the template to the average of the simulation results of all 29 individual datasets. Acoustic simulations were performed for a model of a focused transducer driven at 500 kHz, placed at 24 standardized positions by means of the EEG 10–10 system. Additional simulations at 250 kHz and 750 kHz at 16 of the positions were used for further confirmation. The amount of ultrasound-induced heating at 500 kHz was estimated for the same 16 transducer positions. Our results show that the template represents the median of the acoustic pressure and temperature maps from the individuals reasonably well in most cases. This underpins the usefulness of the template for the planning and optimization of TUS interventions in studies of healthy young adults. Our results further indicate that the amount of variability between the individual simulation results depends on the position. Specifically, the simulated ultrasound-induced heating inside the skull exhibited strong interindividual variability for three posterior positions close to the midline, caused by a high variability of the local skull shape and composition. This should be taken into account when interpreting simulation results based on the template.

1. Introduction

Transcranial focused ultrasound stimulation (TUS) at low intensities is emerging as novel non-invasive neuromodulation method with far better spatial resolution than existing non-invasive stimulation methods and the ability to create three-dimensional foci also in deep brain areas (Bystritsky et al., 2011; Fomenko et al., 2018; Kubanek et al., 2020; Legon et al., 2014; Nakajima et al., 2022; Pasquinelli et al., 2019). The good focality of TUS also comes with the need to accurately control the acoustic wave distribution inside the brain in order to reach a reliable

engagement of the target area. In addition, the stimulation strength needs to be kept within safe, yet neurally effective pressure levels. However, an accurate control of the TUS dose is difficult as the human skull strongly attenuates the wave and distorts its shape (Cain et al., 2021). This effect depends on both the outer shape and internal composition of the skull, which vary between persons and across positions on the head. At many positions, the skull consists of a three-layer structure – an inner layer of spongy bone embedded between outer layers of compact bone (J.-F. Aubry et al., 2003) - while it is only composed of compact bone at its thinnest positions or has a very heterogeneous structure

---

around the sutures. Estimating the TUS acoustic wave transmitted into the brain thus requires detailed numerical simulations informed by computed tomography (CT) or magnetic resonance (MR) data to reach good estimates of the spatial distribution and intensity of the acoustic wave after skull transmission (Montanaro et al., 2021; Mueller et al., 2017; Pasquinelli et al., 2020; J. Robertson et al., 2017).

Individual imaging data is often not available and can be costly. In addition, when exploring and optimizing the TUS intervention during study planning, imaging data of the study participants is often not yet available and using existing individual datasets instead has the challenge that it is unknown how well they represent the population. In this study, we therefore generate a head template from calibrated CT data of 29 healthy individuals of different ages (20-50 years), gender and ethnicity. We then compare key anatomical properties of the template, in particular skull thickness, to the median values of the 29 individual datasets. In addition, we perform a comprehensive set of acoustic simulations at 250, 500 and 750 kHz at several standardized positions on the heads in order to compare the results based on the template to the median of the results of the individual datasets. Finally, we determine how well thermal simulations of the TUS-induced heating based on the template represent the median of the simulation results from the 29 individual datasets. Our results demonstrate that the template-based simulations give a helpful insight into the average acoustic and thermal TUS dose, highlighting the practical relevance of the new template in the planning of future TUS applications.

2. Material and Methods

In this section, we first describe the dataset employed in the study. We then outline how head models for personalized ultrasound simulations were prepared from the CT and MR images, and how the group template was constructed from the CT images of the individual subjects. Subsequently, we provide details of the acoustic and thermal simulations, including the procedures to determine the transducer positions on the heads. Finally, we describe the metrics used to compare the group template with the individual datasets, covering selected anatomical properties and the acoustic and thermal simulation results.

2.1. Dataset

In this study, an existing dataset of CT and MR images of the heads of 29 healthy participants was used. The participants were selected to cover different ages (between 20-50 years old), gender (16 male and 13 female) and ethnicity (15 Caucasian, 13 Asian and 1 African). The CT scan was performed with a Siemens Biograph mCT (PET-CT) with a voxel size of $0.42 \times 0.42 \times 0.6$ mm^3, tube potential of 80 kV and a maximum effective dose below 0.35 mSv for all subjects. In addition, a T1-weighted MR image (3D Turbo Field Echo) was acquired at a 3T Philips Achieva scanner using a 32-channel head coil with a repetition time (TR) of 6 ms, echo time (TE) of 2.7 ms, flip angle (FA) of 8° and an isotropic voxel size of 0.85 mm^3. Further details regarding demographics and scan parameters can be found in (Farcito et al., 2019). The study was approved by the Ethical Committee of the Capital Region of Denmark.

2.2. Preparation of an individual head model

An overview of the complete workflow for preparing an individual head model and performing the acoustic and thermal simulations is shown in Fig. 1A, and the workflow is further explained in the following. As first step, the CT and MR images for the same head were cropped using fslroi (FSL v6.0, Smith et al., 2004) to remove the neck since it was outside the region of interest for this study. The CT and MR images were coregistered and segmented with the complete head anatomy reconstruction method (CHARM; Puonti et al., 2020) to create regional masks of the scalp, compact bone, spongy bone, cranial cavity and inner

air compartments. CHARM also generates a non-linear transformation to the coordinate space of the MNI152 template of the Montreal Neurological Institute (termed "MNI space" in the following), which is used here for determining reproducible transducer positions (further details are given below).

For preparation of the acoustic simulations, values for the material density (ρ), the speed of sound (c) and the acoustic attenuation coefficient (α) were then assigned to the different compartments (Table 1). Unless indicated otherwise, the scalp and cranial cavity were modelled as homogenous water, given the similar acoustic properties of soft tissues and water. In addition, the medium around the head was modelled as homogenous water to simplify the acoustic simulations and ensure adequate coupling between the transducer and the head. As the acoustic wave is focused underneath the transducer, this simplification does not affect the simulation results in our case.

For positions in the compact and spongy bone compartments of the skull, the material density was estimated from the CT Hounsfield units (HU). To accurately determine the relationship between both parameters, an electron density phantom (model 062M, CIRS, Norfolk, VA, USA) with inserts covering a density range from ca. 1000 to 2500 kg/m^3 and a small water container were scanned with the same parameters as used for the CT images of the human heads. The results were used to establish linear relationships between HU and density (J.-F. F. Aubry et al., 2003; Montanaro et al., 2021; Pasquinelli et al., 2020; Stanziola et al., 2022):

$$\rho = s \cdot \mathrm{HU} + \rho_{int} \tag{1}$$

whereby s and ρ_{int} denote the slope and intercept in kg/m^3. Based on the results of the reference measurements (see Fig. 1C), separate relationships were defined for the ranges from $-1000 \leq \mathrm{HU} \leq 0$ and $\mathrm{HU} > 0$. For the range $-1000 \leq \mathrm{HU} \leq 0$, the relationship was established using air (-1000 HU) and water (0 HU) as anchor points, giving a slope $s = 0.9987$ kg/m^3 and an intercept $\rho_{int} = 1000.0$ kg/m^3. For the range $\mathrm{HU} > 0$, a line was fitted to minimize the mean squared error between the predicted and true densities of the inserts of the electron density phantom using the polyfit function in Matlab (The MathWorks, MA, USA). This resulted in a slope $s = 0.4559$ kg/m^3 and an intercept $\rho_{int} = 1003.8$ kg/m^3. Finally, inside the skull, density values below 1000 kg/m^3 caused by spurious noise in the CT images were set to 1000 kg/m^3 (density corresponding to water).

A linear relationship between density and speed of sound was assumed, based on existing literature (J.-F. F. Aubry et al., 2003; Montanaro et al., 2021; Pasquinelli et al., 2020):

$$c = c_{ref1} + \frac{c_{ref2} - c_{ref1}}{\rho_{ref2} - \rho_{ref1}} \left(\rho - \rho_{ref1} \right) \tag{2}$$

Here, air and water were chosen as anchor points $ref1$ and $ref2$. Also other anchor points such as water and skull have been used in previous studies (e.g., Montanaro et al., 2021), moderately changing the linear relationship. However, as this would affect the simulations similarly across all subjects and the template and as our study aims at a relative comparison of template-based versus personalized simulations, this choice is not critical for the purpose of our study.

The acoustic attenuation coefficient of the skull was assumed to be constant, given that a stable and validated mapping of this material property from the CT data is so far missing (Montanaro et al., 2021). In line with this, experimental measurements of the acoustic intensity are often employed to tune the attenuation parameters (J.-F. Aubry et al., 2003; Marquet et al., 2009; J. Robertson et al., 2017).

For the thermal simulations, regional compartments of the scalp, the cranial cavity and the cortical and cancellous bone parts of the skull were created from the segmentation. They were modelled as homogenous materials with spatially constant values of density, speed of sound, thermal conductivity and specific heat capacity (see Table 1). The outer and inner air were modelled as water to simplify the thermal simulations. As most acoustic energy was deposited in regions underneath the

A)

B   **C**   **D**
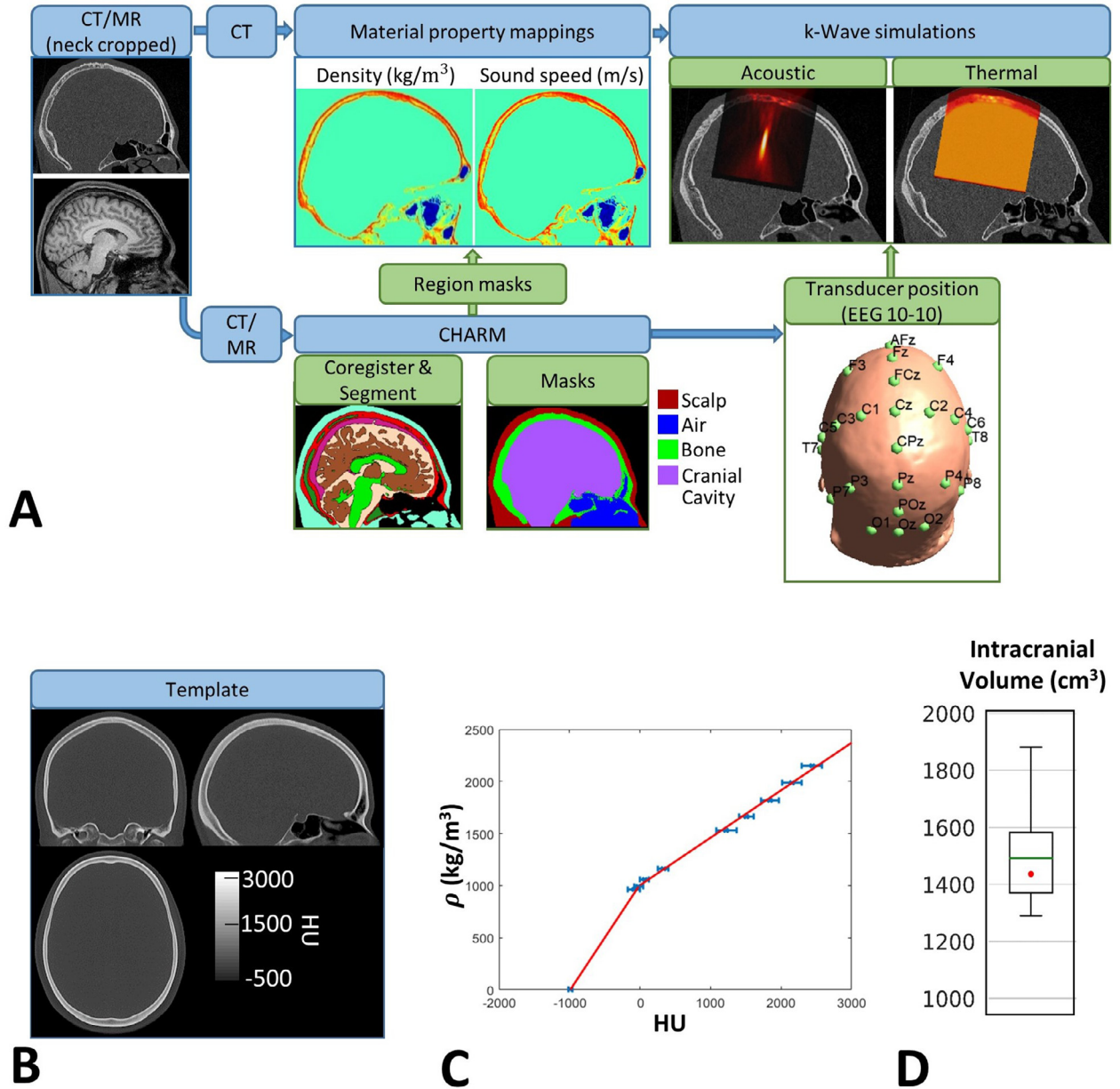
Fig. 1. **A)** TUS simulation workflow. The CT and MR images were fed into SimNIBS CHARM for mutual coregistration, segmentation and non-linear registration to MNI space. The segmentations were used to prepare regional masks for scalp, air, bone (combined compact and spongy bone, unless indicated otherwise) and the skull cavity. With the exception of the skull region, homogenous material properties were assigned to the different regions for the acoustic simulations. The density and speed of sound of the skull bone was estimated from the CT image. In order to obtain standardized transducer positions, 24 positions of the EEG 10–10 standard system were defined in MNI space and transformed to the CT image space of the individual participant using the non-linear registration provided by CHARM. The acoustic and thermal simulations were performed in cylindrical regions of interest (ROIs) under the transducer positions. **B)** Exemplary coronal, sagittal and axial slices of the CT template. **C)** The mapping between CT Hounsfield units (HU) and material density was determined using an electron density phantom having several inserts with varying density, as well as water and air. The blue horizontal lines show the standard deviation around the mean for the HU values in each of the inserts and the water and air ROIs. The red lines show the fitted linear relationships between CT HU and density (two regions, HU < 0 and HU > 0, with different slopes). **D)** Intracranial volume. The boxplot shows the lower and upper quartiles around the median (green line) of the 29 individual data sets. The whiskers indicate the 1.5 times interquartile ranges. The template result is shown as a red dot.

transducer and along its central axis, this simplification does not have a relevant influence on the simulation results.

2.3. Construction of CT Head Template

For creating the template, all CT images were initially cropped to remove the neck part. The script antsMultivariateTemplateConstruction2 of the Advanced Neuroimaging Tools (ANTs) (Avants et al., 2011) was

then run for four iterations using standard settings with affine average, nonlinear registration, cross-correlation as similarity metric, and symmetric normalization as transformation model. The final CT template is shown in Fig. 1B. Similar to the individual datasets, the template was segmented using CHARM to obtain masks of the major tissue compartments (scalp, compact bone, spongy bone, cranial cavity and inner air compartments) and determine a non-linear transformation to the coordinate space of the MNI152 template (the "MNI space").

Table 1

Parameters and values used for acoustic and thermal simulations (Connor and Hynynen, 2004.

Material	$\rho \left(\frac{kg}{m^3}\right)$	$c \left(\frac{m}{s}\right)$	$\alpha \left(\frac{dB}{MHz.cm}\right)$	$k \left(\frac{W}{m.K}\right)$	$C \left(\frac{J}{kg.K}\right)$	$\dot{q}_m \left(\frac{W}{m^3}\right)$		$\omega \left(\frac{1}{s}\right)$
Water (20°C)	1000	1500	36×10^{-4}	0.615	4180	-		-
Air (20°C)	1.275	343	8.99×10^{-4}	-	-	-		-
Brain	1000	1500	36×10^{-4}	0.528	3640	13400		8.3×10^{-3}
Skull	From CT data	From CT data	8.26	0.43	1591	0		3.3×10^{-4}
Scalp	1000	1624	36×10^{-4}	0.34	3530	Skin	368	1.5×10^{-3}
						Fat	58	
Blood	1069	-	-	-	3650	-		-
Cortical bone*	1908	3514.9	-	0.32	1300	-		-
Cancellous bone*	1178	2117.5	-	0.31	1440	-		-

* only used for the thermal simulations (skull in the acoustic simulations)

Table 2

Simulation parameters for three different center frequencies.

Simulation parameter	250 kHz	500 kHz	750 kHz
PPW in water	22	13	9
Grid size (Nx,Ny,Nz)	$335 \times 335 \times 481$	$402 \times 402 \times 524$	$402 \times 402 \times 524$
Spatial discretization (mm)	0.274	0.228	0.228
Temporal discretization (ns)	17	14	14

2.4. Ultrasound Simulations

Simulations were performed for three acoustic frequencies, 250 kHz, 500 kHz and 750 kHz. A focused bowl transducer with a radius of curvature of 64 mm, an aperture diameter of 64 mm and a focal distance of 52 mm was modelled, having broadly similar characteristics as the commercially available transducers for weak transcranial ultrasound stimulation of the human brain. The template-based versus personalized acoustic simulations were compared at 24 transducer positions (Fig. 1A) to cover variations in local skull thickness and composition while maintaining the total number of simulations in a practically manageable range. In order to achieve a reproducible and standardized positioning across all individual CT images and the template, the positions were initially selected from the international 10-10 EEG standard system (Oostenveld et al., 2001) and defined in MNI space. They were then warped from MNI space to the space of the individual (and template, respectively) CT images using the non-linear transformation provided by CHARM. The transducer center was placed at the transformed position and then moved orthogonally to the local head surface to ensure a distance of 10 mm to the skin. The central axis of the transducer was chosen to be orthogonal to the local head surface. For the acoustic frequency of 500 kHz, all 24 transducer positions were used for the simulations. As the results for left-right mirror-symmetric positions (e.g. positions C3 and C4) turned out to be very similar, only the 16 positions from the center line and the left side of the head were chosen for the simulations with 250 kHz and 750 kHz (Fig. 4A top). This helped to reduce the required computational resources without affecting the generalizability of the findings.

The k-Wave toolbox (J. L. B. Robertson et al., 2017) was used for the acoustic simulations and set to solve a linear wave equation in dispersion-free material based on a pseudospectral method (details in chapter 2.1 of (Treeby et al., 2016)). The transducer was modeled as a staircase-free geometry using the kWaveArray class (Wise et al., 2019). Unless specified differently, a 10-cycle tone-burst within an overall time period of 147 μs was simulated. The effect of standing waves was negligible for the chosen length of the tone-burst. The material property maps were linearly interpolated to an isotropic grid with a spacing of 3 points per wavelength (PPW) in air for 500 kHz, 5 PPW for 250 kHz, and 2 PPW for 750 kHz, which was sufficient to ensure the numerical stability of the simulations in the presence of internal air cavities. The resulting PPW in water are listed in Table 2 and are well in the range to achieve good numerical accuracy for the region of the pressure wave. The Courant-Friedrichs-Lewy number was set to 0.2 to have a sufficiently fine temporal resolution for stable simulations (J. L. B. Robertson et al., 2017).

To reduce the computation time, the simulation domain was chopped and rotated during the interpolation step to obtain a volume covering the transducer and its pressure wave and having a z-axis aligned with the central axis of the transducer. A perfectly matched layer (PML) was added to the outer boundaries of the domain and set to 30 grid points to ensure that the reflected waves from the boundaries were absorbed. The resulting grid sizes and spatial resolutions are listed in Table 2 for all three frequencies. Initial comparisons with reference simulations in the non-chopped and non-rotated domain confirmed a close correspondence of the results (data not shown).

2.6. Thermal Simulations

To calculate the temperature increase within the head due to the ultrasound stimulation, simulations of the bio-heat equation (Pennes, 1948) were performed with k-Wave:

$$\nabla(k.\nabla T) + Q = \rho C \frac{\partial T}{\partial t} \tag{3}$$

The temperature is denoted by T, constants k and C are the thermal conductivity and the heat capacity of the material and Q is the volume rate of heat deposition. In the absence of ultrasound stimulation, the metabolic heat generation ($\dot{q}_m$) and heat transfer from blood to tissue (perfusion) ($\dot{q}_p$) are the main contributors to Q (Incropera et al., 1996):

$$Q = \dot{q}_m + \dot{q}_p \tag{4}$$

with $\dot{q}_p = \omega \rho_b C_b (T - T_a)$

Constants ω, ρ_b and C_b are the perfusion rate, density and specific heat capacity of blood, and T_a is the ambient temperature. In case of ultrasound stimulation, the absorbed acoustic power also contributes to Q:

$$Q = \dot{q}_m + \dot{q}_p + Q_{acoustic} \tag{5}$$

with $Q_{acoustic} = \alpha \frac{P^2}{\rho c}$, where P is the pressure obtained in the acoustic simulations. The material properties used for the thermal simulations are listed in Table 1. For the thermal simulations, homogeneous values of density, speed of sound, thermal conductivity, and specific heat capacity for cortical and cancellous bone were considered.

Three different cases were considered in the thermal simulations: a) Ultrasound-induced heating (pressure from individual simulations) with metabolic generated heat and blood perfusion: The individual pressure maps at 500 kHz acoustic frequency were rescaled to obtain a focal peak pressure of 1 MPa. This case relates to a usage scenario where the stimulation intensity is adjusted according to the individual simulation results. b) Ultrasound-induced heating (pressure based on template simulations) with metabolic generated heat and blood perfusion: The individual pressure maps at 500 kHz acoustic frequency were rescaled by the factor required to obtain a focal peak pressure of 1 MPa in the template simulations. This relates to a scenario where the stimulation intensity is adjusted according to the template simulation results, e.g. when individual imaging data is not available. c) Baseline with only metabolic generated heat and blood perfusion. It was included here as control for the temperature changes during the simulation period that were unrelated to the application of the ultrasound. This baseline case was added as ultrasound was applied directly at the start of the simulations in cases a and b, so that the tissue temperatures were not yet fully within their steady state (details see below). In order to isolate ultrasound-specific temperature changes, the results of case c were subtracted from those of cases a and b, respectively, in the further analyses. As note, the temperature differences to steady state were generally small and the above analysis approach did not affect the general conclusions compared to analyses based only on cases a and b.

For all cases, the initial temperature for different tissues and surrounding medium were set to 37.4 °C, 35.2 °C, 33.2 °C, and 24 °C for the cranial cavity, skull, scalp, and medium, respectively. These values correspond to the average steady state values in these regions for the baseline case. However, as the same temperature value was assigned to all parts of a tissue compartment (i.e. temperatures were piecewise spatially constant), the simulations were not fully in steady state yet, and case c controls for the extent of that effect. This approach was also validated with a single-subject simulation of an ultrasound-induced heating starting from steady state.

All simulations with ultrasound-induced heating were executed with 4s on-time (time step of 10ms) and 40s off-time (time step of 100ms) for acoustic source. The baseline case had a corresponding duration of 44 s. As for the acoustic simulations with 250 kHz and 750 kHz, only the 16 transducer positions from the center line and the left side of the head were used for the thermal simulations in order to reduce the required computational resources.

2.7. Comparison Metrics

The template was compared to the individual CT images using the following metrics that assessed relevant anatomical properties and the results of the acoustic and thermal simulations:

- Anatomical properties: 1) The intracranial volume was determined from the corresponding regional mask provided by CHARM. 2) The thicknesses of skull and scalp under the transducer positions were calculated. For that, the scalp and bone masks were rotated so that the z-axis of the interpolated volumes were aligned with the central axis of the transducer. The thicknesses of scalp and skull were then determined in 2D columns along the z-direction and used to calculate average thickness values in cylindrical regions-of-interest (ROIs) of a diameter of 60 mm and a length of 80 mm underneath the transducer. The ROI size was selected to cover the regions of increased acoustic pressure inside the scalp, skull and the cranial cavity. 3) Histograms of skull density were determined in the same cylindrical volumes.
- Acoustic simulation results: 1) The intracranial peak pressure was determined for each transducer position and normalized by the peak pressure in free water. 2) The volume of the full-width-at-half-maximum (FWHM) was determined for the intracranial pressure maps. 3) The misalignment of the peak pressure location from

the central axis of the transducer was determined by calculating the angular deviation between a line from the transducer center to the peak pressure location and the central axis of the transducer.
- Thermal simulation results were assessed inside the cylindrical ROIs underneath the transducer positions. This was done after the TUS on-time of 4s and again at the end of the simulated cooling phase after 44s: 1) Peak temperatures were determined separately for the cranial cavity, the skull and the scalp. 2) Mean temperatures were determined in the same subvolumes. 3) The peak temperature differences relative to the baseline case without ultrasound were determined in the same subvolumes.

Box plots were used to descriptively compare to the template results to the results of all participants. In addition, the strength of the linear relationships between the template results and median of the population results were determined using Pearson's correlation coefficient and t-tests.

3. Results

3.1. Anatomical properties

The template moderately underestimates the median of the population for intracranial volume, but falls well within the interquartile range (Fig. 1D) and its intracranial volume falls well within the range reported in prior studies (Abbott et al., 2000; Kruggel, 2006). The skull thickness of the template is consistently slightly higher than the population median (Fig. 2A). However, the template values are within the interquartile range, except for position T8, and the deviations from the median are generally small (Table 3). Importantly, the systematic differences in skull thickness that occur between positions (e.g. lower thicknesses for T7 and T8 compared to C1, Cz and C2) are well captured by the template, as confirmed by a strong correlation between the population median and the template value across positions (Fig. 7A). The deviations in scalp thickness of the template from the population median are small as well (Fig. 2B, Table 3), and are far smaller than the differences in scalp thickness that occur across positions (e.g. high thicknesses for T7 and T8). The systematic variations across positions are again well captured by the template (Fig. 7B).

Visual comparison of the histograms of the skull densities indicates that high density values corresponding to compact bone (~1500-2000 kg/m^3) were generally well maintained in the template (Figure S1). This suggests that the template building process achieved a good registration of the two outer skull layers consisting of compact bone across the different datasets. Correspondingly, the outer skull layers of the template are visible as well-defined lines of increased intensity with a sharp transition towards soft tissue in Fig. 8. On the other hand, localized peaks in the histograms in the lower density range corresponding to spongy bone (~1000-1500 kg/m^3) occurred at some head positions for the template, but were absent in the average histograms of the 29 datasets. We suggest that interindividual differences in the density of spongy bone get "averaged out" during template building, resulting in a smaller range of densities for spongy bone in the template that shows up as peak in the histogram. Overall, the skull density ranges fit well to the values reported in prior literature (Delye et al., 2015; Marsac et al., 2017; J. Robertson et al., 2017).

3.2. Acoustic simulations

The results of the acoustic simulations for 500 kHz are summarized in Fig. 3. The corresponding correlation plots between the population median and the template value across the 24 positions are shown in Fig. 7C-E (black lines and circles). The template values deviate more from the population median for the acoustic results than for the basic anatomical properties reported above and fall often outside the interquartile range. However, they still capture the systematic differences
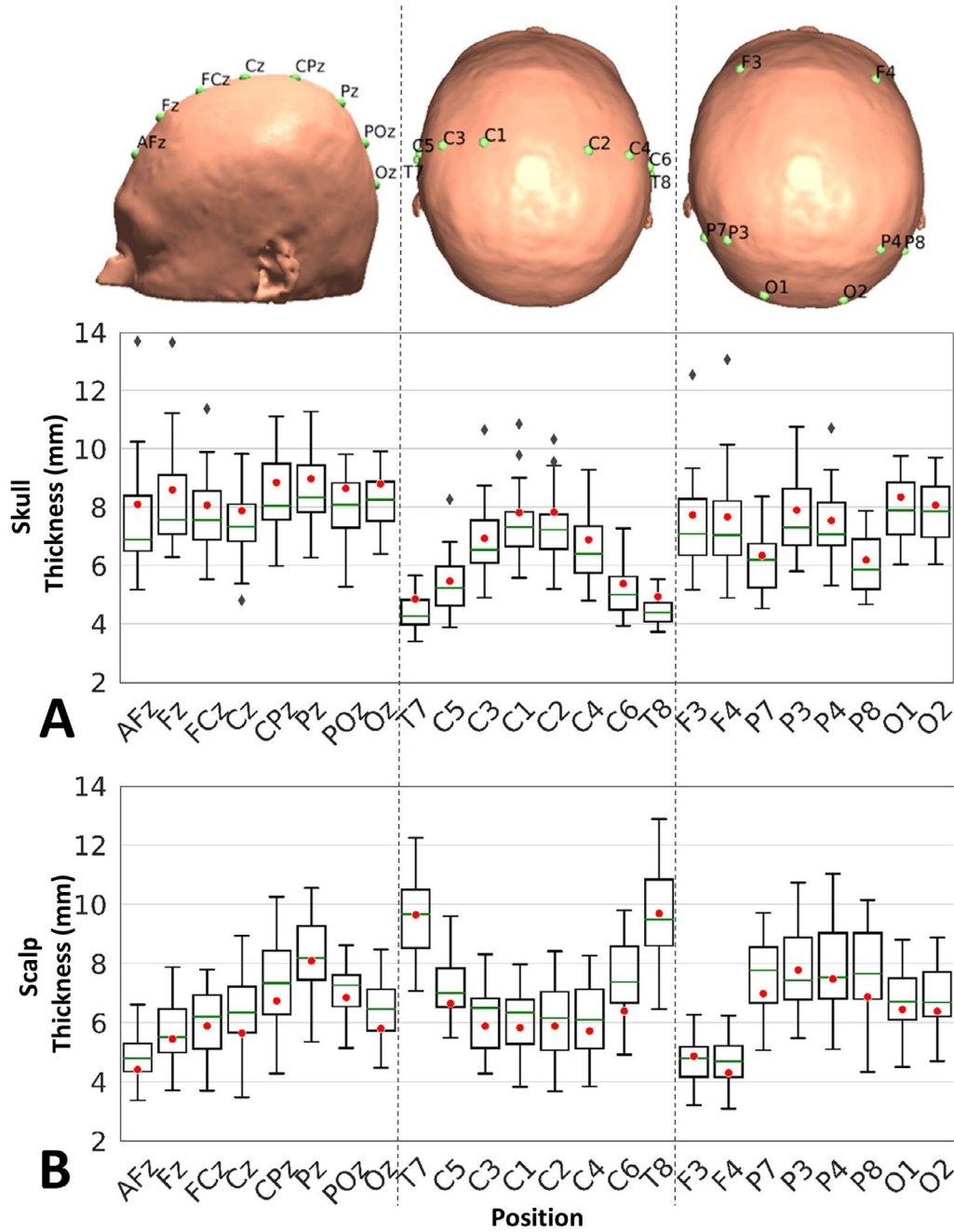
Fig. 2. A) Skull, and **B)** scalp thickness for the 24 transducer positions. The boxplots show the lower and upper quartiles around the median (green lines) of the 29 individual data sets. The whiskers indicate the 1.5 times interquartile ranges. The template results are shown as red dots.

that occur between positions, as confirmed by significant correlations. On average, the deviations of the template values from the population median are around 15% for the normalized peak pressure and 21% for the FWHM volume (Table 3). The angular deviations are low in general, rendering also the deviations of the template values from the population median of limited practical relevance.

As expected, comparing the acoustic simulation results for 500 kHz (Fig. 3) with those for 250 kHz and 750 kHz (Fig. 4) shows a general decrease of the normalized peak pressure with increasing frequency and an increase in focality. The template values capture the systematic differences that occur between positions also for 250 kHz and 750 kHz, as confirmed by significant correlations (Fig. 7C-E, blue and red lines). For the normalized peak pressure, the average deviations of the template values from the population median for the 16 simulated positions are

around 12% and 18% at 250 and 750 kHz, respectively. For the FWHM volume, the corresponding average deviations are around 14% and 32%. These deviations are in similar ranges compared to those observed for 500 kHz. The angular deviations remain generally low also for 250 kHz and 750 kHz.

The transmitted acoustic wave is affected by the local skull shape and composition underneath the transducer in a complex way, making it unlikely that differences between the simulation results based on individual data and the template can be attributed to a single parameter. For illustration, Fig. 8 shows the acoustic waves for positions Oz and POz that exhibit clear interindividual variations of both the local shape of the inner skull boundaries and the density of the spongy bone. The individual simulation results having the highest and lowest intracranial pressures and the template results are depicted. Low intracranial pres-

Table 3

Population median and interquartile range (IQR) and median of the absolute differences between the template result and the population median for anatomical properties, acoustic simulations, and thermal simulations (heating periods only). In addition, the maximal absolute differences between the template result and the population median and the corresponding transducer position are reported. The results for 500 kHz acoustic frequency were determined from all 24 positions. For the frequencies of 250 kHz and 750 kHz and the thermal simulations, the results were determined from 16 positions (see Fig. 4A top).

	Parameter	Population Median/IQR	Absolute Difference		
			Median/IQR	Maximal value	Position with maximal value
500 kHz	Skull thickness (mm)	7.01/2.11	0.87/0.83	5.59	AFz
	Skin thickness (mm)	6.76/2.40	0.91/1.12	3.56	P4
	Normalized peak pressure	0.39/0.09	0.06/0.07	0.35	C6
	FWHM vol. (mm^3)	413.5/232.9	87.2/169.1	2179.5	AFz
	Angular Deviation (°)	1.00/0.93	0.47/0.64	7.05	Fz
250 kHz	Normalized peak pressure	0.47/0.13	0.06/0.07	0.27	P7
	FWHM vol. (mm^3)	2281.0/832.5	325.4/449.5	3595.5	POz
	Angular Deviation (°)	0.81/0.81	0.39/0.44	9.10	Oz
750 kHz	Normalized peak pressure	0.31/0.11	0.07/0.09	0.31	CPz
	FWHM vol. (mm^3)	196.7/208.5	64.1/137.7	1631.2	P7
	Angular Deviation (°)	1.03/1.09	0.52/0.83	9.09	Cz
Case a	Cranial cavity (°C)	0.15/0.49	0.10/0.36	2.78	Pz
	Skull (°C)	4.07/3.40	1.41/2.09	21.1	Oz
	Scalp (°C)	1.22/0.87	0.47/0.61	3.79	O1
Case b	Cranial cavity (°C)	0.12/0.57	0.08/0.44	2.11	POz
	Skull (°C)	3.85/2.97	0.88/1.40	18.41	Oz
	Scalp (°C)	1.15/0.97	0.33/0.46	2.48	POz

sures coincide with a more complex inner skull boundary and a lower density of the spongy bone, causing a splitting of the transmitted wave into two parts and a complex standing wave pattern inside the skull.

3.3. Thermal simulations

The peak temperature differences inside the cranial cavity, skull and scalp compared to the baseline case without ultrasound are reported for cases in which the intracranial peak pressure was set to 1 MPa based on the results of the individual acoustic simulations (case a in Fig. 5) and the template simulations (case b in Fig. 6), respectively.

There is generally little ultrasound-induced heating inside the cranial cavity and only moderate heating in the scalp. The latter is particularly seen for transducer positions Pz, POz and Oz, and visual inspection revealed that it occurred at positions close to the skull and was caused by heat conducted from the skull. Expectedly, the strongest temperature increase occurs inside the skull as it strongly attenuates the ultrasound wave. For the skull, the template values capture the systematic differences in the population median across the 16 positions reasonable well, as confirmed by significant correlations (Figure 7F&G, black lines and circles). Also the median deviations of the template values from the population median are in reasonable ranges (Table 3). However, there is notable interindividual variability in the amount of peak temperature increase in particular for positions Pz, POz and Oz, and a strong increase in the peak temperature in one of the individuals.

We additionally determined the mean temperature increases inside the scalp, skull and cranial cavity parts within the cylindrical ROIs under the transducers. Generally, the mean temperature increase in the cranial cavity and scalp remained robustly below 1°C in all cases and was therefore not analyzed further. The results for the skull confirm the findings observed for the peak temperatures, namely that the template results represent the population median reasonably well, but that strong heating occurs in some of the individual for positions Pz, POz and Oz (Fig. S2). However, the highest increase in the mean temperature remained under 3° in all cases.

4. Discussion

In this study, a head template was created from calibrated CT images of 29 healthy adults of varying age, gender and ethnicity. The template

was comprehensively validated for use in simulations of the acoustic wave and the thermal effects of transcranial focused ultrasound stimulation. By comparing anatomical measures obtained for the template to the median of the 29 individual results, it was first confirmed that the template adequately represented the average head anatomy of the individual datasets. In particular, the systematic differences in the median scalp and skull thicknesses between the 24 tested transducer positions were well captured by the template. Second, comparisons of the acoustic simulation results confirmed that the template-based estimates reproduced the position-dependent variations of the intracranial peak pressure, the volume and the direction of the acoustic wave well, in general. The template-based acoustic simulations deviated from the population median sufficiently little to ensure the practical relevance of the template in the planning of future TUS applications. Third, this conclusion was again confirmed for simulations of the TUS-induced heating, in particular inside the skull, on a subset of 16 transducer positions. Our work complements a prior study (Rorden et al., 2012) that generated a CT head template for the older population (median age 65 years). In contrast to that study, we here aimed at providing a template specifically for TUS simulations in younger adults. Therefore, we based the template on calibrated CT data for participants between 20 and 50 years age to obtain accurate estimates of the skull density and comprehensibly validated the anatomical properties of the template and its performance in acoustic and thermal simulations.

The averaging procedure inherent in the template-building process (Avants et al., 2011) reduces the spatial high-frequency content in the CT images. This decreases the imaging noise, but also removes information about the individually unique porous structures of the inner skull layer (Fig. 8). As result, histograms of the bone density revealed that the template represents the high density range corresponding to the two outer layers of compact bone well, but that the inner skull layer of the template consists of a more confined density range than observed for the varying spongy bone compartments of the individuals. However, we find it unlikely that this effect explains the remaining deviations of the template-based simulation results from the population median. For example, the normalized peak pressure for position C5 is overestimated for 250 kHz, underestimated for 500 kHz and slightly overestimated for 750 kHz again (Figures 3A, 4A&D). This error pattern is too complex to be explained by a consistent misestimation of the porosity of the inner skull by the template. In addition, we ran exploratory analyses that
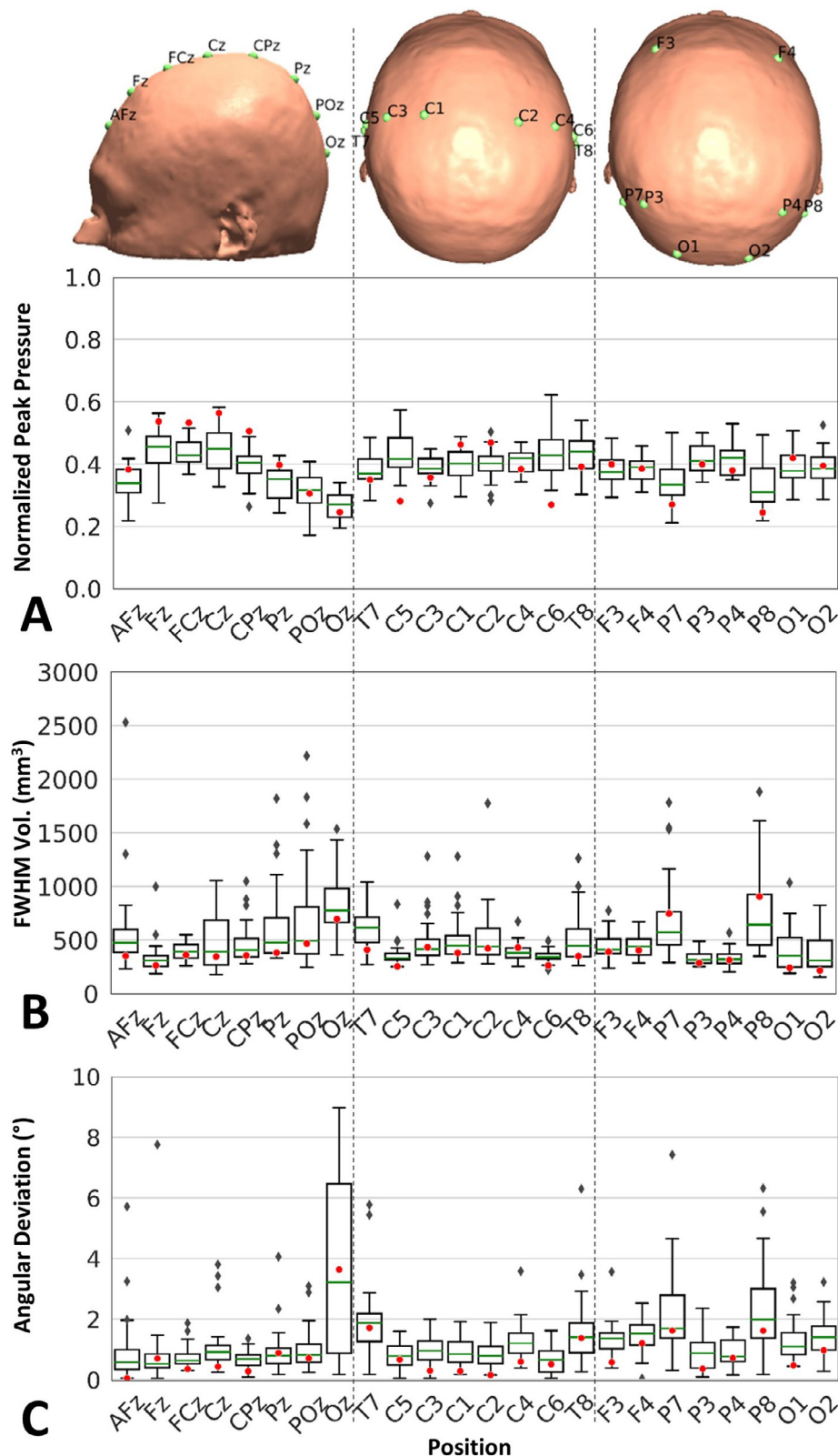
Fig. 3. A) Normalized peak pressure, **B)** FWHM volume, and **C)** angular deviation of the acoustic simulation results at 500 kHz. The results are restricted to positions within the cranial cavity. The boxplots show the lower and upper quartiles around the median (green lines) of the 29 individual data sets. The whiskers indicate the 1.5 times interquartile ranges. The template results are shown as red dots.

aimed to relate the remaining position-dependent deviations to the local skull or scalp thickness, which did not give conclusive results (data not shown). Thus, we suggest that the remaining deviations cannot be attributed to a single straightforward cause.

Related to the above topic, it should be noted that we assumed a constant acoustic attenuation for bone, because a validated and generally accepted mapping from CT HU to attenuation is so far still missing

(Montanaro et al., 2021). By that, the effects of interindividual differences of bone porosity on the pressure wave were reduced, which might have resulted in an underestimation of the true interindividual variability of the TUS acoustic wave after skull transmission (e.g., Chen et al., 2023; Marsac et al., 2017; McDannold et al., 2019; Pichardo and Hynynen, 2007; Riis et al., 2022). In addition, the differences in the amount of bone porosity between the template and the individual CT scans might
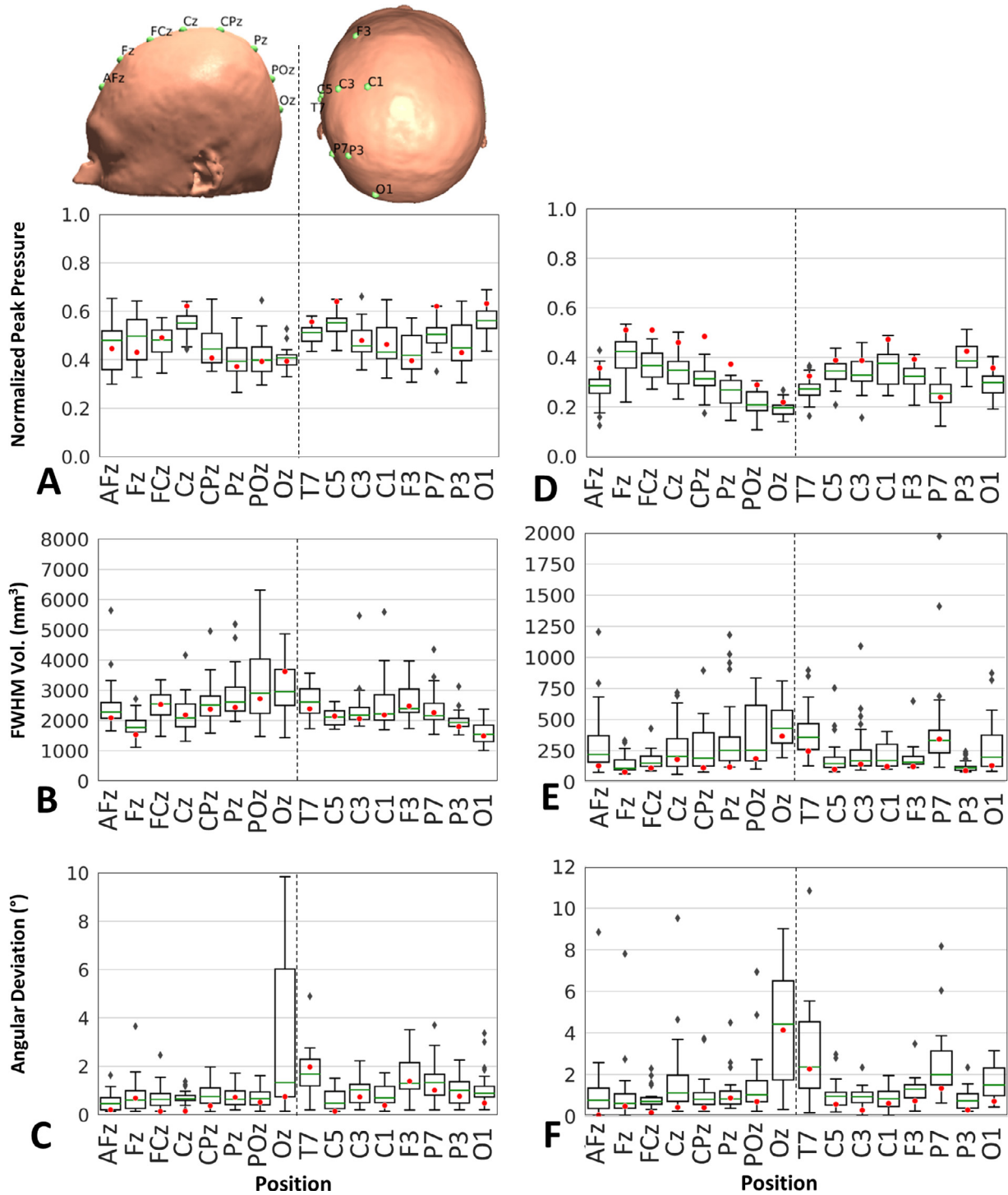
Fig. 4. Acoustic simulation results for 250 kHz and 750 kHz for 16 transducer positions (indicated in the inset on the top). **A&D)** Intracranial peak pressure, **B&E)** FWHM volume and **C&F)** angular deviation. The boxplots show the lower and upper quartiles around the median (green lines) of the 29 individual data sets. The whiskers indicate the 1.5 times interquartile ranges. The template results are shown as red dots.

become more relevant once acoustic attenuation is estimated from CT HU, indicating that the performance of the template should be reevaluated in that case.

Knowledge about the expected amount of variability between the individual simulation results is important for the interpretation of the template-based simulations. This is because, even when the template results serve as a reasonable estimate of the population median, they do not allow insight into the likelihood of strong deviations in some of the subjects. Our results showed that the interindivdual variability

varied with both the transducer position and the applied measure. This is most relevant for measures related to TUS safety such as the estimated peak pressure which showed only few high outliers, i.e. individuals in which the pressure was much stronger than the template estimates (worst cases had roughly two times the peak pressure of the template). In contrast, the estimated heating (most pronounced in the skull) had strong interindividual variability and high outliers that strongly exceeded the template results for two of the 16 tested transducer positions (Pz and POz, the latter being above the cruciform eminence that shows
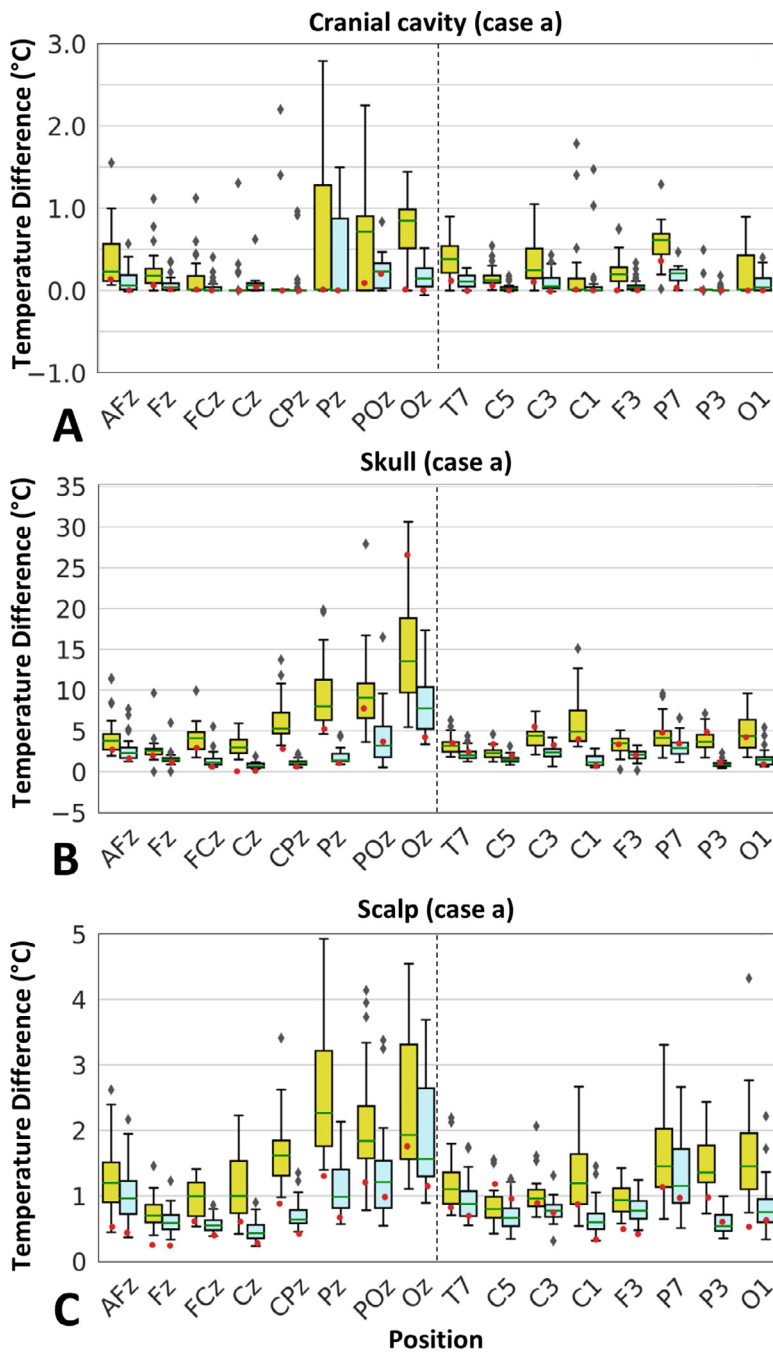
Fig. 5. Peak temperature differences for thermal simulations informed by the acoustic results for 500 kHz, relative to the baseline case (case c) without stimulation. The results for **case a** are shown, which refers to the scenario in which the peak pressure in the cranial cavity of 1 MPa was determined from individual simulations for 500 kHz. The peak temperature difference are shown for **A)** the cranial cavity, **B)** skull, and **C)** scalp. The peak temperature differences were recorded after an ultrasound-induced heating of 4 s (yellow color) and after 40 s of cooling (light blue). The boxplots show the lower and upper quartiles around the median (green lines) of the 29 individual data sets. The whiskers indicate the 1.5 times interquartile ranges. The template results are shown as red dots.
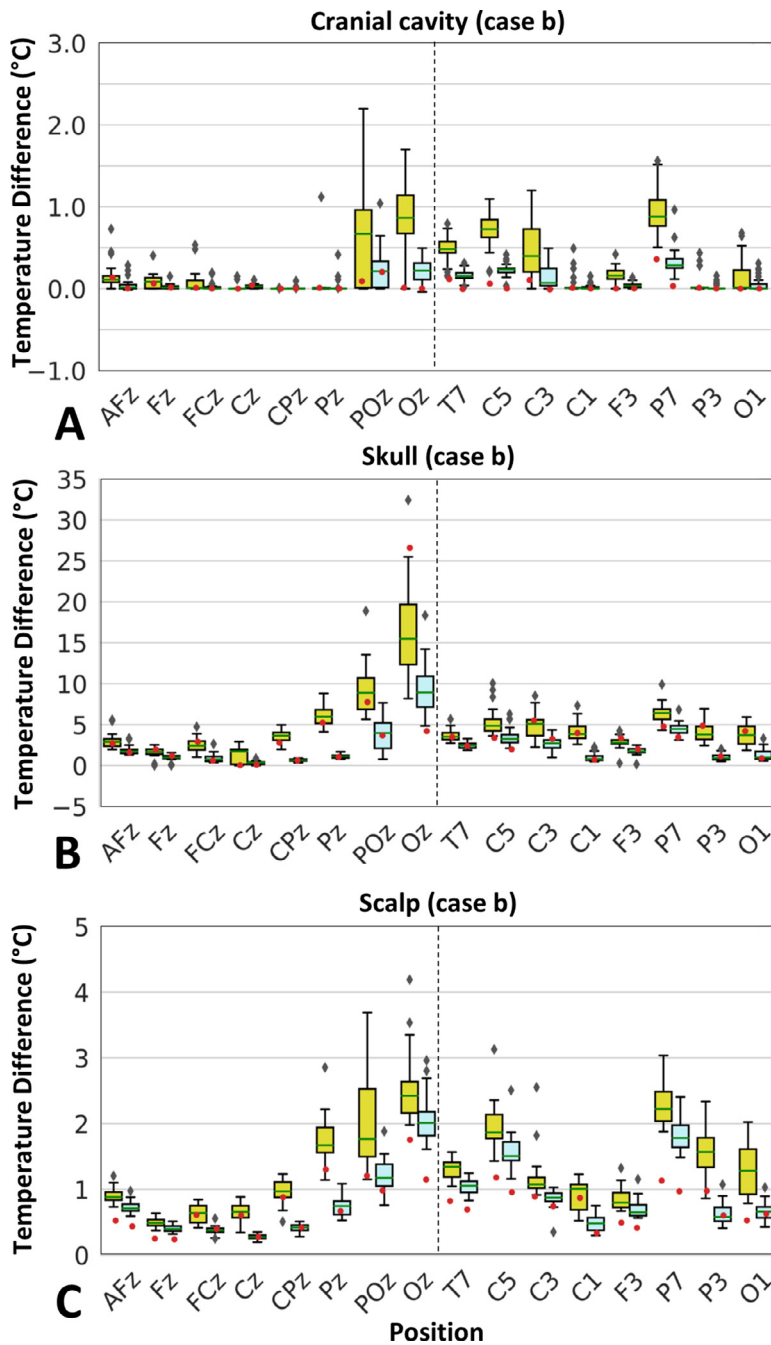
Fig. 6. Peak temperature differences for thermal simulations informed by the acoustic results for 500 kHz, relative to the baseline case (case c) without stimulation. The results for **case b** are shown, which refers to the scenario in which the peak pressure in the cranial cavity of 1 MPa was determined from template simulations for 500 kHz. The peak temperature difference are shown for **A)** the cranial cavity, **B)** skull, and **C)** scalp. Please see the legend for Fig. 5 for further details.

strong anatomical variability between participants). Interestingly, visual inspection of the outliers with a strong heating of the skull revealed that the individual skull shape and high skull thickness (similar to the lowest pressure cases shown in Fig. 8) resulted in a localized energy deposition at some positions inside the spongy bone of the skull. Given the low density of spongy bone compared to compact bone (Pichardo et al., 2010), this led to a particularly high local heating. This was more pronounced for "case a", as a high ultrasound intensity was needed to counteract the strong attenuation caused by the individual skull in order to obtain the desired peak pressure of 1 MPa inside the cranial cavity in that case. These results suggest that, as the peak temperature in the skull is influenced by local properties of the skull shape and composition, it will exhibit more interindividual variability compared to the intracranial peak pressure for some transducer positions such as those close to the occipital pole.

In conclusion, TUS simulations based on our template head represent the median of the individual simulation results well enough, both for the acoustic pressure wave and the related heating effects, to be useful in the planning and optimization of TUS studies. In particular, the template-based results reproduce the systematic dependencies on transducer position and ultrasound frequency that occur for the median of the individual results. Knowledge of the expected interindividual variability around the median is important for interpreting simulations based on a group template. Future studies could aim to link the amount of interindividual variability of the local skull shape and composition to the variability of the simulation results in order to gain systematic insight into the head regions that provide the most reliable TUS targeting. Once a validated and stable mapping from CT HU to acoustic attenuation is available, it would be relevant to update our results accordingly to obtain a better estimate of the interindividual variability of the TUS
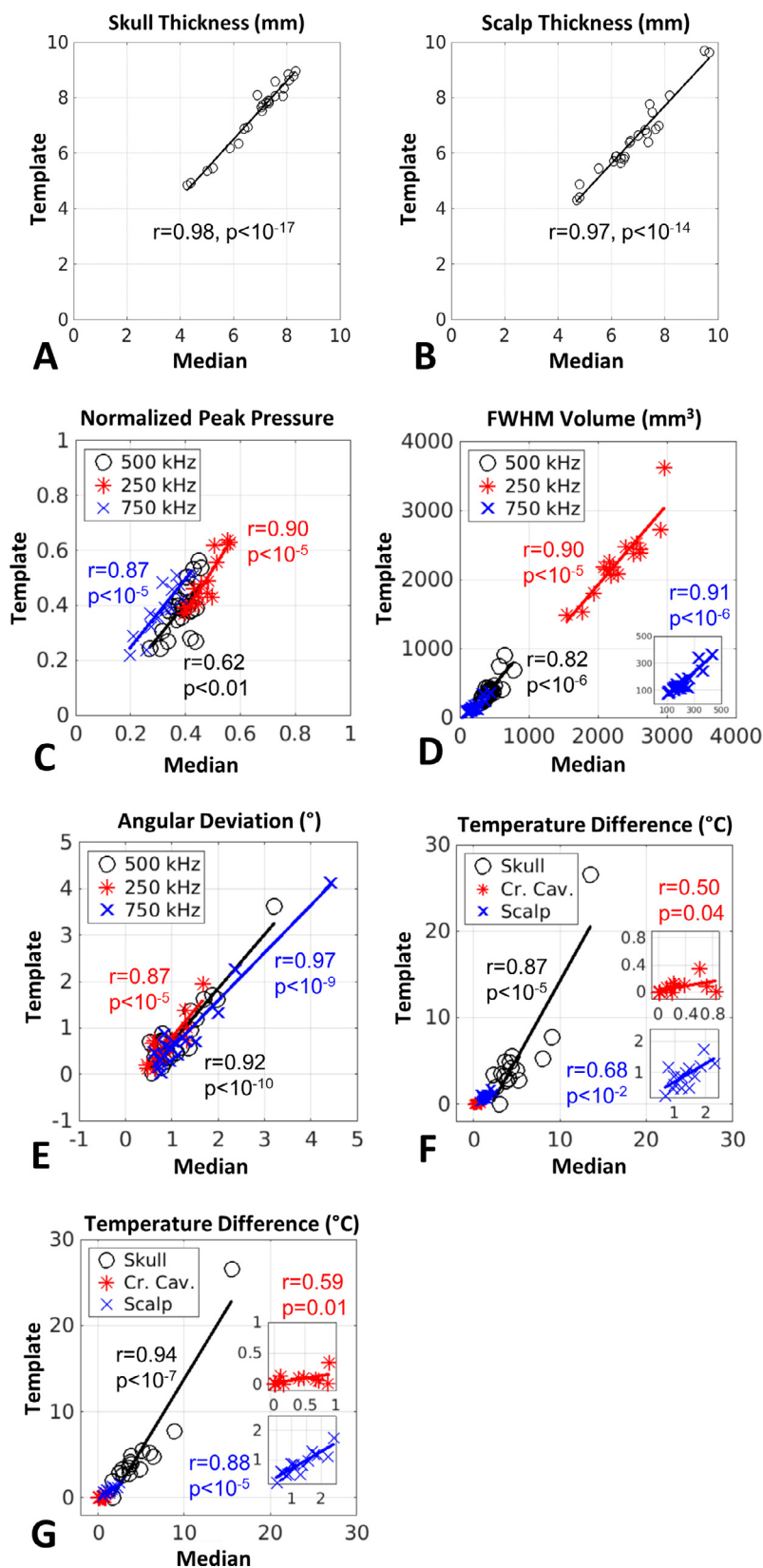
Fig. 7. Correlation analyses between the results for the template and for the median of the 29 individual data sets. **A&B)** Thicknesses of skull and scalp. **C)** Normalized intracranial peak pressure, **D)** FWHM volume, and **E)** angular deviation. The results for 500 kHz are based on simulations for 24 transducer positions. The results for 250 kHz and 750 kHz are based on simulations for 16 transducer positions. **F&G)** Peak temperature differences relative to baseline for cases a and b, respectively. All results are stated without correction for multiple comparisons.
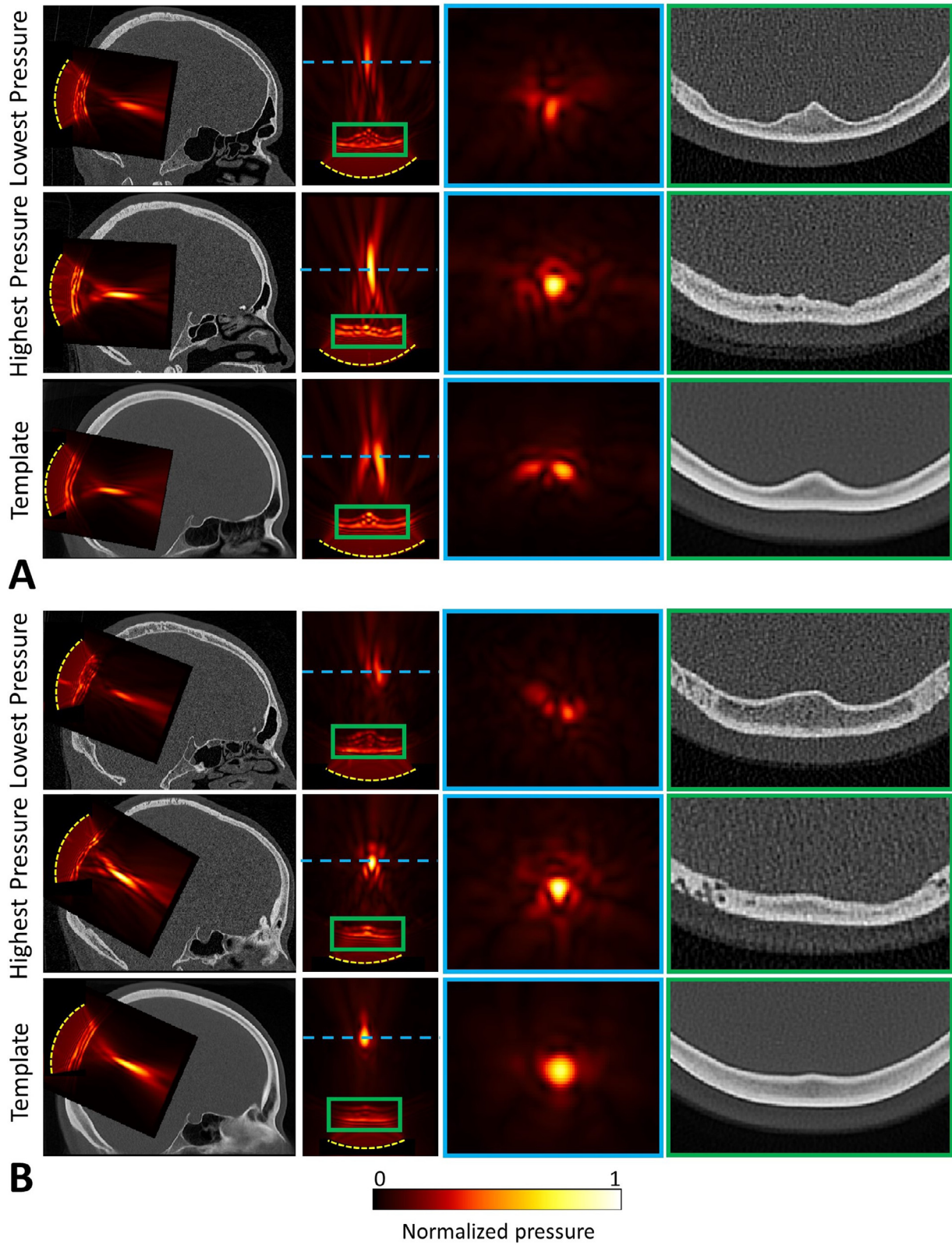
Fig. 8. Visual representation of the propagated acoustic beam for 500 kHz acoustic frequency through the skull and after passing it for transducer positions at **A)** Oz and **B)** POz for the two subjects with the lowest and highest intracranial pressure for these positions and the template. The columns (from left to right) show the acoustic wave overlaid on the individual CT image (sagittal view), the acoustic wave (axial view), the acoustic wave (coronal slice, position indicated as blue dashed line in the second column) and the skull (axial slice, position indicated as green box in the second column).

acoustic wave after skull transmission and to confirm the validity of the proposed head template.

Data and code availability

The template with relevant auxiliary data is made publicly available for download. The scripts for generating the template and for performing and analyzing the ultrasound simulations were developed to address our immediate research needs, but not for broader dissemination and will therefore not be made publicly available. They may still be obtained from the authors upon reasonable request. The MR and CT data cannot be made available due to privacy restrictions.

Declaration of Competing Interest

None.

Credit authorship contribution statement

Seyedsina Hosseini: Methodology, Software, Formal analysis, Investigation, Writing – original draft, Visualization. **Oula Puonti:** Conceptualization, Methodology, Software, Formal analysis, Writing – review & editing. **Bradley Treeby:** Conceptualization, Methodology, Software, Writing – review & editing. **Lars G. Hanson:** Conceptualization, Methodology, Investigation, Writing – review & editing, Supervision. **Axel Thielscher:** Conceptualization, Methodology, Investigation, Writing – review & editing, Supervision, Funding acquisition.

Data availability

The authors do not have permission to share data.

Supplementary materials

Supplementary material associated with this article can be found, in the online version, at doi:10.1016/j.neuroimage.2023.120227.

References

Abbott, A.H., Netherway, D.J., Niemann, D.B., Clark, B., Yamamoto, M., Cole, J., Hanieh, A., Moore, M.H., David, D.J., 2000. CT-determined intracranial volume for a normal population. J. Craniofac. Surg. 11, 211–223.

Aubry, J.-F., Tanter, M., Pernot, M., Thomas, J.-L., Fink, M., 2003a. Experimental demonstration of noninvasive transskull adaptive focusing based on prior computed tomography scans. J. Acoust. Soc. Am. 113, 84–93. doi:10.1121/1.1529663.

Aubry, J.-F.F., Tanter, M., Pernot, M., Thomas, J.-L.L., Fink, M., 2003b. Experimental demonstration of noninvasive transskull adaptive focusing based on prior computed tomography scans. J. Acoust. Soc. Am. 113, 84–93. doi:10.1121/1.1529663.

Avants, B., Tustison, N., Song, G., Cook, P., Klein, A., 2011. A reproducible evaluation of ANTs similarity metric performance in brain image registration. NeuroImage.

Bystritsky, A., Korb, A.S., Douglas, P.K., Cohen, M.S., Melega, W.P., Mulgaonkar, A.P., Desalles, A., Min, B.K., Yoo, S.S., 2011. A review of low-intensity focused ultrasound pulsation. Brain Stimulat. 4, 125–136. doi:10.1016/J.BRS.2011.03.007.

Cain, J.A., Visagan, S., Johnson, M.A., Crone, J., Blades, R., Spivak, N.M., Shattuck, D.W., Monti, M.M., 2021. Real time and delayed effects of subcortical low intensity focused ultrasound. Sci. Rep. 111 (11), 1–14. doi:10.1038/s41598-021-85504-y.

Chen, M., Peng, C., Wu, H., Huang, C.-C., Kim, T., Traylor, Z., Muller, M., Chhatbar, P.Y., Nam, C.S., Feng, W., Jiang, X., 2023. Numerical and experimental evaluation of low-intensity transcranial focused ultrasound wave propagation using human skulls for brain neuromodulation. Med. Phys. 50, 38–49. doi:10.1002/mp.16090.

Connor, C.W., Hynynen, K., 2004. Patterns of thermal deposition in the skull during transcranial focused ultrasound surgery. IEEE Trans. Biomed. Eng. 51 (10), 1693–1706.

Delye, H., Clijmans, T., Mommaerts, M.Y., Sloten, J.V., Goffin, J., 2015. Creating a normative database of age-specific 3D geometrical data, bone density, and bone thickness of the developing skull: a pilot study. J. Neurosurg. Pediatr. 16, 687–702. doi:10.3171/2015.4.PEDS1493.

Farcito, S., Puonti, O., Montanaro, H., Saturnino, G., Nielsen, J., Madsen, C., Siebner, H., Neufeld, E., Kuster, N., Lloyd, B., Thielscher, A., 2019. Accurate anatomical head segmentations: a data set for biomedical simulations. Annu. Int. Conf. IEEE Eng. Med. Biol. Soc. 2019.

Fomenko, A., Neudorfer, C., Dallapiazza, R.F., Kalia, S.K., Lozano, A.M., 2018. Low-intensity ultrasound neuromodulation: an overview of mechanisms and emerging human applications. Brain Stimulat. 11, 1209–1217. doi:10.1016/J.BRS.2018.08.013.

Incropera, F., DeWitt, D., Bergman, T., Lavine, A., 1996. Fundamentals of heat and mass transfer.

Kruggel, F., 2006. MRI-based volumetry of head compartments: normative values of healthy adults. Neuroimage 30, 1–11. doi:10.1016/j.neuroimage.2005.09.063.

Kubanek, J., Brown, J., Ye, P., Pauly, K.B., Moore, T., Newsome, W., 2020. Remote, brain region-specific control of choice behavior with ultrasonic waves. Sci. Adv. 6. doi:10.1126/SCIADV.AAZ4193.

Legon, W., Sato, T.F., Opitz, A., Mueller, J., Barbour, A., Williams, A., Tyler, W.J., 2014. Transcranial focused ultrasound modulates the activity of primary somatosensory cortex in humans. Nat. Neurosci. 172 (17), 322–329. doi:10.1038/nn.3620, 2013.

Marquet, F., Pernot, M., Aubry, J.F., Montaldo, G., Marsac, L., Tanter, M., Fink, M., 2009. Non-invasive transcranial ultrasound therapy based on a 3D CT scan: protocol validation and in vitro results. Phys. Med. Biol. 54, 2597. doi:10.1088/0031-9155/54/9/001.

Marsac, L., Chauvet, D., La Greca, R., Boch, A.-L., Chaumoitre, K., Tanter, M., Aubry, J.-F., 2017. *Ex vivo* optimisation of a heterogeneous speed of sound model of the human skull for non-invasive transcranial focused ultrasound at 1 MHz. Int. J. Hyperthermia 33, 635–645. doi:10.1080/02656736.2017.1295322.

McDannold, N., White, P.J., Cosgrove, R., 2019. Elementwise approach for simulating transcranial MRI-guided focused ultrasound thermal ablation. Phys. Rev. Res. 1, 033205. doi:10.1103/PhysRevResearch.1.033205.

Montanaro, H., Pasquinelli, C., Lee, H.J., Kim, H., Siebner, H.R., Kuster, N., Thielscher, A., Neufeld, E., 2021. The impact of CT image parameters and skull heterogeneity modeling on the accuracy of transcranial focused ultrasound simulations. J. Neural Eng. 18, 46041. doi:10.1088/1741-2552/abf68d.

Mueller, J.K., Ai, L., Bansal, P., Legon, W., 2017. Numerical evaluation of the skull for human neuromodulation with transcranial focused ultrasound. J. Neural Eng. 14, 066012. doi:10.1088/1741-2552/aa843e.

Nakajima, K., Osada, T., Ogawa, A., Tanaka, M., Oka, S., Kamagata, K., Aoki, S., Oshima, Y., Tanaka, S., Konishi, S., 2022. A causal role of anterior prefrontal-putamen circuit for response inhibition revealed by transcranial ultrasound stimulation in humans. Cell Rep. 40, 111197. doi:10.1016/J.CELREP.2022.111197.

Oostenveld, R., Praamstra, P., 2001. The five percent electrode system for high-resolution EEG and ERP measurements. Clin. Neurophysiol..

Pasquinelli, C., Hanson, L.G., Siebner, H.R., Lee, H.J., Thielscher, A., 2019. Safety of transcranial focused ultrasound stimulation: a systematic review of the state of knowledge from both human and animal studies. Brain Stimulat 12, 1367–1380. doi:10.1016/J.BRS.2019.07.024.

Pasquinelli, C., Montanaro, H., Lee, H.J., Hanson, L.G., Kim, H., Kuster, N., Siebner, H.R., Neufeld, E., Thielscher, A., 2020. Transducer modeling for accurate acoustic simulations of transcranial focused ultrasound stimulation. J. Neural Eng. doi:10.1088/1741-2552/ab98dc.

Pennes, H.H., 1948. Analysis of tissue and arterial blood temperatures in the resting human forearm. J. Appl. Physiol. 1, 93–122. doi:10.1152/JAPPL.1948.1.2.93.

Pichardo, S., Hynynen, K., 2007. Treatment of near-skull brain tissue with a focused device using shear-mode conversion: a numerical study. Phys. Med. Biol. 52, 7313. doi:10.1088/0031-9155/52/24/008.

Pichardo, S., Sin, V.W., Hynynen, K., 2010. Multi-frequency characterization of the speed of sound and attenuation coefficient for longitudinal transmission of freshly excised human skulls. Phys. Med. Biol. 56, 219. doi:10.1088/0031-9155/56/1/014.

Puonti, O., Van Leemput, K., Saturnino, G., Siebner, H., Madsen, K., Thielscher, A., 2020. Accurate and robust whole-head segmentation from magnetic resonance images for individualized head modeling. Neuroimage 219, 117044.

Riis, T.S., Webb, T.D., Kubanek, J., 2022. Acoustic properties across the human skull. Ultrasonics 119, 106591. doi:10.1016/j.ultras.2021.106591.

Robertson, J., Martin, E., Cox, B., Treeby, B.E., 2017a. Sensitivity of simulated transcranial ultrasound fields to acoustic medium property maps. Phys. Med. Biol. 62, 2559–2580. doi:10.1088/1361-6560/aa5e98.

Robertson, J.L.B., Cox, B.T., Jaros, J., Treeby, B.E., 2017b. Accurate simulation of transcranial ultrasound propagation for ultrasonic neuromodulation and stimulation. J. Acoust. Soc. Am. 141, 1726. doi:10.1121/1.4976339.

Rorden, C., Bonilha, L., Fridriksson, J., Bender, B., Karnath, H.O., 2012. Age-specific CT and MRI templates for spatial normalization. Neuroimage 61, 957–965. doi:10.1016/J.NEUROIMAGE.2012.03.020.

Smith, S.M., Jenkinson, M., Woolrich, M.W., Beckmann, C.F., Behrens, T.E.J., Johansen-Berg, H., Bannister, P.R., Luca, M.D., Drobnjak, I., Flitney, D.E., Niazy, R.K., Saunders, J., Vickers, J., Zhang, Y., Stefano, N.D., Brady, J.M., Matthews, P.M., 2004. Advances in functional and structural MR image analysis and implementation as FSL. Neuroimage 23, S208–S219.

Stanziola, A., Pineda-Pardo, J.A., Treeby, B., 2022. Transcranial ultrasound simulation with uncertainty estimation. arXiv:2212.04405.

Treeby, B., Cox, B., Jaros, J., 2016. A MATLAB toolbox for the time domain simulation of acoustic wave fields - k-wave User Manual v. 1.1.

Wise, E.S., Cox, B.T., Jaros, J., Treeby, B.E., 2019. Representing arbitrary acoustic source and sensor distributions in Fourier collocation methodsa). J. Acoust. Soc. Am. 146, 278. doi:10.1121/1.5116132.